Heliyon 9 (2023) e17662

Contents lists available at ScienceDirect

Heliyon

journal homepage: www.cell.com/heliyon

# Enabling hydrate-based methane storage under mild operating conditions by periodic mesoporous organosilica nanotubes

Emile Jules Beckwée [a,1], Geert Watson [b,1], Maarten Houlleberghs [c,1], Daniel Arenas Esteban [d], Sara Bals [d], Pascal Van Der Voort [b], Eric Breynaert [c], Johan Martens [c], Gino V. Baron [a], Joeri F.M. Denayer [a,*]

[a] Department of Chemical Engineering, Vrije Universiteit Brussel, Pleinlaan 2, 1050, Brussel, Belgium
[b] Center for Ordered Materials, Organometallics and Catalysis, Department of Chemistry, Ghent University, Krijgslaan 281, B-9000, Ghent, Belgium
[c] Centre for Surface Chemistry and Catalysis, NMRCoRe - NMR - XRAY - EM Platform for Convergence Research, Department of Microbial and Molecular Systems (M2S), KU Leuven, Celestijnenlaan 200F, 3001, Leuven, Belgium
[d] Electron Microscopy for Materials Science, Department of Physics, University of Antwerp, Groenenborgerlaan 171, 2020, Antwerp, Belgium

ARTICLE INFO

*Keywords:*
Biomethane
Clathrate hydrate
Methane hydrate
Periodic mesoporous organosilica
Pressure-swing (un)loading

ABSTRACT

Biomethane is a renewable natural gas substitute produced from biogas. Storage of this sustainable energy vector in confined clathrate hydrates, encapsulated in the pores of a host material, is a highly promising avenue to improve storage capacity and energy efficiency. Herein, a new type of periodic mesoporous organosilica (PMO) nanotubes, referred to as hollow ring PMO (HR-PMO), capable of promoting methane clathrate hydrate formation under mild working conditions (273 K, 3.5 MPa) and at high water loading (5.1 g water/g HR-PMO) is reported. Gravimetric uptake measurements reveal a steep single-stepped isotherm and a noticeably high methane storage capacity (0.55 g methane/g HR-PMO; 0.11 g methane/g water at 3.5 MPa). The large working capacity throughout consecutive pressure-induced clathrate hydrate formation-dissociation cycles demonstrates the material's excellent recyclability (97% preservation of capacity). Supported by ex situ cryo-electron tomography and x-ray diffraction, HR-PMO nanotubes are hypothesized to promote clathrate hydrate nucleation and growth by distribution and confinement of water in the mesopores of their outer wall, along the central channels of the nanotubes and on the external nanotube surface. These findings showcase the potential for application of organosilica materials with hierarchical and interconnected pore systems for pressure-based storage of biomethane in confined clathrate hydrates.

## 1. Introduction

A key factor in decarbonizing the energy and transportation sectors is the availability of renewable energy sources such as biogas, a product of anaerobically digested (waste) biomass primarily consisting of 50–70% methane ($CH_4$) and 30–50% carbon dioxide ($CO_2$) [1]. Physicochemical upgrading of biogas through pressure swing adsorption, membrane separation, and physical and chemical absorption can increase the $CH_4$ content above 97%, thus effectively improving the Lower Caloric Value from 20 to 25 MJ $m^{-3}$ to 36 MJ

* Corresponding author.
*E-mail address:* joeri.denayer@vub.be (J.F.M. Denayer).
[1] Co-first authorship.

https://doi.org/10.1016/j.heliyon.2023.e17662
Received 31 May 2023; Received in revised form 14 June 2023; Accepted 25 June 2023
Available online 28 June 2023

$m^{-3}$ $CH_4$ (at 273 K, 100 kPa) [1]. High-caloric purified biogas is referred to as biomethane, a non-intermittent, non-fossil-based natural gas (NG) substitute.

Current natural gas storage technologies are predominantly based on compression to 25 MPa at 298 K (CNG) or cryogenic liquification at 111 K and 0.1 MPa (LNG), rendering safe and energy-efficient storage of methane a major technological bottleneck. In recent years, there has been an increasing interest in solidified natural gas storage (SNG), storing methane in methane clathrate hydrates [2]. Methane clathrate hydrates, also referred to as methane hydrates, are ice-like inclusion compounds with a host lattice composed of different cages formed exclusively by hydrogen-bonded water molecules. These cages are large enough to occlude non-polar guest molecules, including methane, through van der Waals interactions with the host structure [3]. In nature, vast amounts of methane hydrate are found in permafrost regions and in ocean sediments at continental borders. It is estimated that between 2.13 $10^{15}$ kg and 2.40 $10^{15}$ kg of methane is trapped within these natural hydrate deposits [4–7]. Apart from naturally occurring methane hydrate, which could potentially serve as a major energy source, synthetic methane hydrates, formed by contacting water and methane under strictly controlled (high) pressure and (low) temperature conditions (up to 10 MPa at 274.2 K), bear great promise as storage technology [2].

Methane hydrates typically adopt a structure I hydrate crystal structure, comprising a cubic unit cell assembly of 2 small and 6 large cages. The structure of each cage is denoted by two digits, i.e. $X^n$, X being a polygonal face lining the cage wall and n the number of X faces lining the cage wall. The small cage in a structure I clathrate hydrate is composed of 12 pentagonal faces ($5^{12}$) and has a radius of 0.395 nm. The large cages consist of 12 pentagonal faces and 2 hexagonal faces ($5^{12}6^2$) and have a radius of 0.433 nm. In theory, each cage can accommodate one methane molecule, leading to a unit cell stoichiometry of 8 $CH_4 \cdot 46H_2O$ and a maximum gravimetric storage capacity of 15.5 wt% methane [3,8]. Hydrate formation, however, is a slow process, especially when starting from bulk water systems. Initial hydrate films at the liquid-gas interface can be formed relatively fast, but as the film reaches a thickness of 0.1 mm, methane diffusion through the film slows down and becomes rate limiting, decreasing the hydrate growth rate by up to two orders of magnitude [9]. This drawback can be overcome by adding kinetic and/or thermodynamic promoters to the aqueous phase to promote hydrate nucleation and growth. Kinetic promoters are often surface-active compounds which migrate to the liquid-gas interface and alter the surface properties of the liquid, enhancing the solubility and diffusion rate of otherwise poorly soluble molecules [10]. Addition of 300 ppm of sodium dodecyl sulphate (SDS) for instance was shown to increase methane uptake rates by a factor of 6 compared to pure water at 273.15 K and 7.0 MPa methane pressure [11]. Thermodynamic promoters are known to lower the nucleation pressure and/or to increase the required temperature. This type of promoter includes cyclic organic compounds such as cyclopentane (CP) and tetrahydrofuran (THF) [2]. Lee et al. observed that addition of 5.6 mol% of CP raised the equilibrium temperature for nucleation at 5 MPa to 300 K, which is 20 K higher than an unpromoted methane hydrate [12]. Similarly, addition of 5.6 mol% of THF was shown to promote methane hydrate formation in less than 4 min at 283 K and 7.2 MPa, whereas only a thin film of hydrate was observed at 274 K and 9.5 MPa in the absence of THF [13]. Despite their obvious advantages, the use of promoters comes at the expense of the overall storage capacity as the promoter molecules typically occupy the large hydrate cages.

Promotion of hydrate nucleation and growth in absence of secondary guests has been achieved by confining the water phase to pores and interparticle voids of nanoporous host materials. Activated carbons [14–24], metal-organic frameworks [25–29], zeolites [30–33], polymers [34,35], and silica-based materials [36–54] have been shown to positively impact hydrate formation kinetics. Pore size and surface chemistry/hydrophobicity have been put forward as key properties determining the solid host's promoting role on hydrate nucleation conditions, stability, and growth/dissociation rates [55–57]. A systematic study by Borchardt et al. on high-pressure methane uptake on wetted micro-, meso- and macroporous carbons, has shown mesopores with a pore size of 25 nm to be superior in both storage capacity and nucleation and growth rate at 264 K and 8.5 MPa $CH_4$ [22]. Generally, micropores (<2 nm) are too small to host structure I hydrates (unit cell lattice: 1.2 nm), leading to slow hydrate formation from microdroplets on the external surface of the adsorbent [22,25], while macropores are inferred to insufficiently disperse the water phase to benefit from the improved contact surface [22]. The promoting role of moderate hydrophobic surfaces on hydrate formation [14,46,53,54,58,59] has been linked to higher gas densities and less distorted tetrahedral water orientations near the surface [56,57,59].

In this respect, Periodic Mesoporous Organosilicas (PMOs) form an interesting, yet peculiar class of mesoporous materials which can exhibit high surface areas and pore volumes, upwards of 2300 $m^2\ g^{-1}$ and 1.9 $cm^3\ g^{-1}$, respectively [60,61]. Unlike their pure silica counterparts such as SBA-15, PMOs are formed through the condensation of bis-silylated organosilicon monomers, resulting in the incorporation of organic moieties throughout the framework. This organic nature results in dramatically increased hydrothermal and chemical stabilities [62]. Additionally, the presence of organic moieties opens up unique windows of opportunities to further fine tune the surface chemistry through choice of monomers and post functionalization methods. The porosity of the final PMO material can easily be adjusted by changing the synthesis conditions. Common methods include the variation of structure directing agents (SDA) and addition of pore swelling agents to alter the pore connectivity and increase pore size, respectively [63,64].

To the best of our knowledge, this study is the first to report a detailed and quantitative study of the equilibrium and kinetics of methane hydrate formation as promoted by the presence of ring PMO structured in a hollow nanotube morphology, hereafter called hollow ring PMO (HR-PMO). The material's promoting capacity on methane hydrate formation is studied at multiple water loadings and temperatures by dynamic high-pressure gravimetric measurements. The applicability of wetted HR-PMO as storage medium is evaluated through multiple pressure-induced formation-dissociation cycles. The presence and distribution of structure I methane hydrate throughout the samples is confirmed by PXRD and further supported by cryo-scanning transmission electron tomography measurements.

## 2. Materials and methods

### 2.1. HR-PMO synthesis

Cetylammoniumbromide (CTAB), $NH_{3(aq)}$ (25%), ethanol (EtOH), acetone, $HCl_{(aq)}$ (37%) and tetraethyl orthosilicate (TEOS) were purchased from ChemLab. Pluronic F-127 was purchased from Merck Life Science. The organosilane 1,1,3,3,5,5–hexaethoxy-1,3,5-trisilacyclohexane (HETSCH) was purchased from Gelest. All chemicals were used without any additional purification. A flask was charged with $H_2O$ (145 ml) and $NH_{3(aq)}$ (5 ml), to which CTAB (1.5 g), Pluronic F-127 (0.615 g) were added as SDAs. The whole was mixed at room temperature until a clear solution was observed. A silica core is grown around the SDA template upon the addition of TEOS (1.5 ml, 7.7 mmol), after which the mixture was left to stir for 1 h at room temperature. The organosilica shell is grown around the previously formed silica core through the addition of HETSCH (1.5 ml, 3.7 mmol) after which the whole was left to stir for two more hours. Finally, the flask was placed in an oven for 48 h at 373 K to complete the organo-silica network condensation, after which a white solid was collected through filtration. Unreacted silanes and surfactants were removed by dispersing the solid in a solution containing EtOH (300 ml) and $HCl_{(aq)}$ (3.5 ml), left to reflux for 24 h. The final material, denoted as HR-PMO, was obtained through a second filtration step during which the solid was washed extensively with EtOH until neutral pH. Residual solvent was removed through heating at 393 K at reduced pressure (5 mbar) for 12 h. A synthesis procedure diagram can be found on Fig. S1.

### 2.2. HR-PMO characterization

Diffuse Reflectance Infrared Fourier Transform Spectroscopy (DRIFTS) measurements were recorded on a Nicolet 6700 spectrometer (Thermo Scientific) in a KBr matrix. Two-dimensional transmission electron microscopy (2D TEM) pictures were taken using a JEOL JEM-1010 TEM instrument without spherical aberration (cs) correction operated at 100 kV. High-Angle Annular Dark-Field Scanning Transmission Electron Microscopy (HAADF-STEM) images and both room temperature (RT) and cryo-electron tomography has been performed on an aberration-corrected cubed Thermo Fisher Titan microscope operating at 300 kV. 3D reconstructions were obtained using the Expectation Maximization (EM) algorithm implemented in Astra Toolbox [65,66]. Further details on the tomography procedure and 3D reconstruction are provided in Supporting Information Section S2. The powder X-ray diffraction (PXRD) pattern was measured on a Bruker D8 Advance with autochanger using Cu K-alpha irradiation with a wavelength (λ) of 0.154 nm in a Bragg-Brentano geometry. Micro- and mesoporosity were assessed volumetrically by argon (Ar) physisorption at 87 K recorded on a 3P Micro 200 instrument. The Brunauer Emmett Teller (BET) specific surface area was calculated adopting the guidelines laid out by Rouquerol et al. [67–69]. The pore size distribution and total pore volume were derived from the Ar adsorption branch by non-local density functional theory (NLDFT), assuming cylindrical pores and a silica/zeolite matrix (fitting error: 0.349%). Macroporosity was measured by two mercury intrusion/extrusion cycles measured on a Fisons Instruments Porosimeter 2000 (0.1–200.0 MPa) equipped with a Pascal 140 unit (0.01–0.20 MPa), adopting a mercury wetting angle of 141.3° and surface tension of 480 mN/m. The skeletal volume of the sample was determined by 10 He displacement experiments on a Micromeritics AccuPyc 1330 pycnometer. Prior to adsorption, intrusion or gas displacement, samples were outgassed under vacuum at 393 K for 12 h. Thermogravimetric analysis (TGA) in a nitrogen ($N_2$) atmosphere was performed using a Stanton Redcroft 1500 device and showed 393 K to be sufficient to remove adsorbed water, while not deteriorating the material (Fig. S2). A water vapor adsorption isotherm was measured at 303 K by the gravimetric principle on a VTI Corporation SGA-100H instrument using $N_2$ as carrier gas. Prior to the isotherm measurement, the sample was degassed under 200 Nml $min^{-1}$ $N_2$ while heating at 2 K $min^{-1}$ to 373 K, maintaining this temperature for 4 h. The silanol content was determined using quantitative $^1H$ MAS NMR spectroscopy in combination with standard addition of water, explained in detail in Section S4 of Supporting Information [70].

### 2.3. High-pressure methane storage: equilibrium and kinetics

High-pressure methane uptake measurements were performed using an in-house developed gravimetric device, based on a Rubotherm magnetic suspension balance connected to an in-house developed gas dosage system operated by LabVIEW software. The instrument is equipped with Keller pressure transducers ensuring quantification between vacuum and 15 MPa with an accuracy of 0.05%. The measurement temperature is controlled between 243 K and 343 K within 0.01 K by use of a Julabo Dyneo DD-1000F circulation thermostat. The unique feature of this device is that it allows to simultaneously determine the kinetics of methane hydrate formation and the equilibrium isotherm in a quantitative and accurate way.

Methane uptake measurements were performed on dry and wet samples at 273, 267 and 248 K. Dry samples were degassed in situ under vacuum at 373 K for 12 h. Wet samples were prepared by activating 0.1 g of HR-PMO ex situ under vacuum at 373 K for 12 h in 10 mL glass vials, before adding MilliQ water dropwise until the desired fractional water loading ($R_w = mass_{H_2O}/mass_{PMO}$) was reached and transferring the sample to the stainless-steel sample container of the balance. A buoyancy experiment, to correct mass readings for the buoyancy force acting on the sample and its container, was performed each time a new sample was loaded. A more detailed description of the buoyancy measurement procedure is provided in Supporting Information Section S5. Isotherm measurements on dry and wet samples were performed by incrementally dosing methane to the sample cell and measuring the mass change, while controlling the temperature. Methane uptake is expressed on a gravimetric basis normalized to the sample's water content or mass of activated adsorbent.

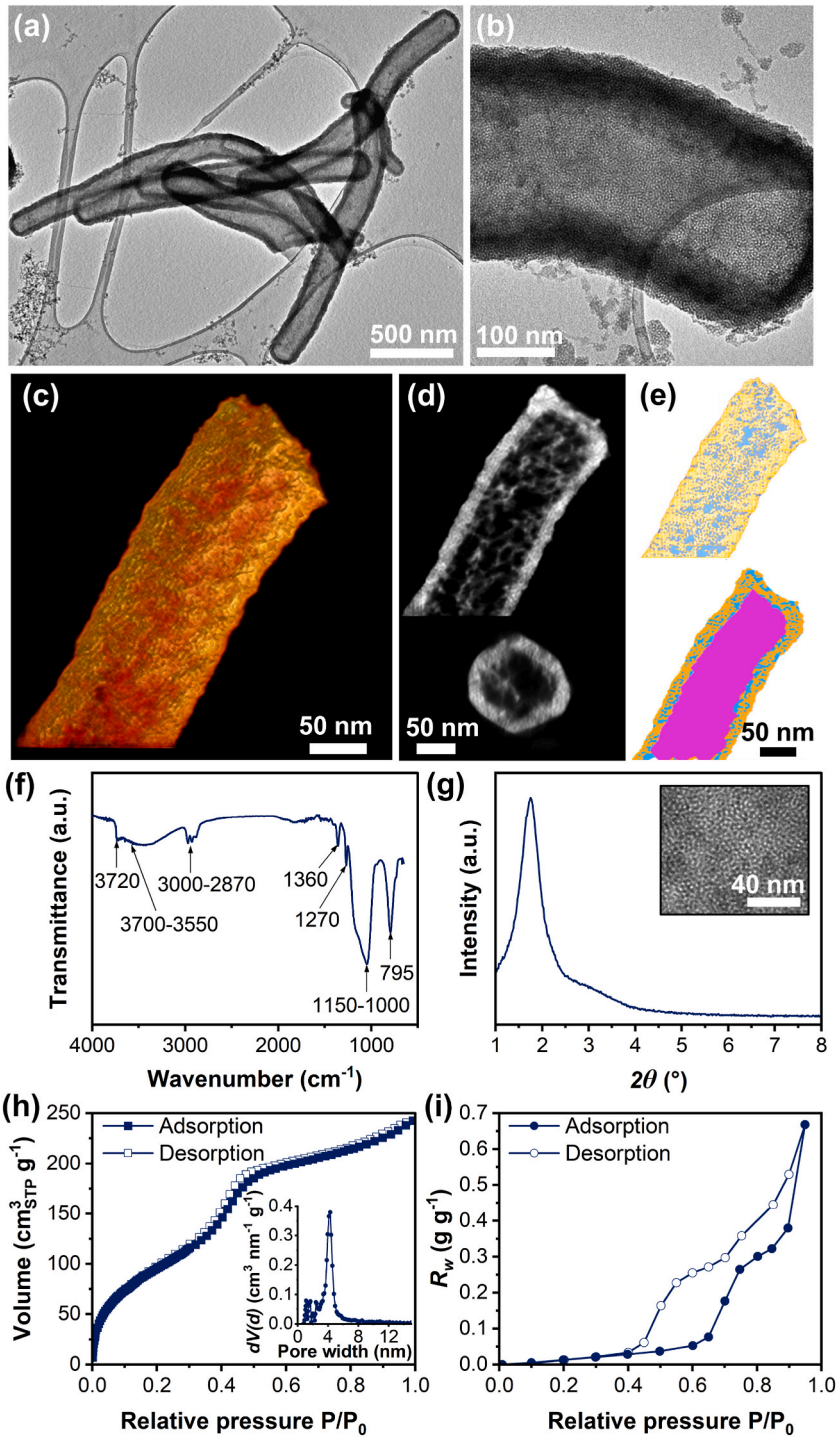


**Fig. 1.** Electron microscopy-based characterization of HR-PMO nanotubes: a, b) 2D TEM images, c) 3D rendering of the outcome of the HAADF-STEM tomography, d) respective orthoslices acquired along perpendicular directions of the 3D reconstruction and e) illustration of the segmented 3D volume and an orthoslice through the dataset, showing the internal cavity, wall pores and ring PMO in pink, blue and orange, respectively. Chemical and textural characterization of HR-PMO: f) DRIFTS spectrum, g) XRD spectrum with a TEM picture inset showing the ordering of mesopores in the particle wall, h) argon adsorption/desorption isotherm at 87 K with NLDFT-based pore size distribution as inset, i) water vapor adsorption/desorption isotherm at 303 K. (For interpretation of the references to colour in this figure legend, the reader is referred to the Web version of this article.)

$$q^{W}_{CH_4} = \frac{m_{CH_4}}{m_{H_2O}} * 100 \quad (1)$$

$$q^{A}_{CH_4} = \frac{m_{CH_4}}{m_{PMO}} * 100 \quad (2)$$

With $q^{W}_{CH_4}$ the methane capacity relative to the sample's water content, hereafter called the gravimetric hydrate storage capacity (wt %), $m_{CH_4}$ the surface excess methane uptake (g), $m_{H_2O}$ the sample's mass of water (g), $q^{A}_{CH_4}$ the methane capacity relative to the dry adsorbent mass, hereafter called the dry weight storage capacity (wt%) and $m_{PMO}$ the sample's mass of activated adsorbent (g). The derivations of equations (1) and (2) are given in Supporting Information section S5, along with the calculations for hydrate and total storage capacity expressed on a volumetric basis.

### 2.4. X-ray diffraction of confined methane hydrate

The crystal structure of the clathrate hydrate formed in the presence of HR-PMO was characterized by X-ray diffraction. To ensure stability of the hydrate phase at atmospheric pressure, an existing XRD sample holder was modified with Kapton® to enable operation at liquid nitrogen ($LN_2$) temperature, i.e. 77 K. Methane hydrate containing samples formed at 273 K and 7.0 MPa were first ground in a mortar filled with $LN_2$ and then transferred to the sample holder which had been submerged in $LN_2$ up until the transfer. PXRD data were recorded using a B STOE STADI P Combi diffractometer with focusing Ge(111) monochromator ($CuK_{\alpha 1}$ radiation, $\lambda = 0.154$ nm) in a high throughput set-up in transmission geometry. Data was collected using a 140°-curved image plate position sensitive detector (IP PSD) from 0 to 62.5° 2Θ.

### 2.5. Room temperature and cryo-electron tomography

HAADF-STEM images and tilt series for electron tomography are recorded under different conditions for empty and clathrate bearing samples. The empty samples were dispersed in ethanol at room temperature and drop cast on an amorphous carbon coated Cu TEM grid. On the other hand, for the sample containing the clathrate the synthesis reactor was opened in liquid nitrogen and the sample was loaded onto a Cu TEM grid by immersing it in the liquid nitrogen dispersion. The sample was introduced into the microscope at liquid nitrogen temperature and kept at this low temperature during the TEM experiment.

Also, the acquisition of the tilt series was performed in a different manner for empty and clathrate loaded samples, due to the sensitivity of the latter to the electron beam. For the empty sample, a conventional electron tomography tilt series was acquired. However, for the sample loaded with the clathrate, imaged at liquid nitrogen, an incremental fast acquisition method was employed [71]. More technical details on the difference between conventional and fast tomography are provided in Supporting Information Section S2. For the sample with the clathrate, a dedicated cryo-tomography holder was used to reduce beam damage and protect the clathrate hydrate from melting while observing.

## 3. Results and discussion

### 3.1. HR-PMO characterization

The combined growth-etching synthesis procedure resulted in a fine white powder of HR-PMO with a low apparent density, as shown in Fig. S5. Infrared spectroscopy (DRIFTS) shows well-defined archetypal peaks and bands of an organosilicon compound (both C–H and Si–OH, Si–O stretching) (Fig. 1f) (Detailed discussion can be found in Supporting Information Section S7). 2D transmission electron microscopy (TEM) images reveal a complex, tubular/rod-shaped morphology of HR-PMO particles closed at both ends (Fig. 1a). The internal tube diameter ranges from 72 to 245 nm, with an average diameter of 151 nm. Closer inspection of the particle walls illustrates the porous nature of the PMO material, i.e. cylindrical mesopores, showing up as lighter dots, oriented perpendicular to the central channel of the nanotubes (Fig. 1b). Structurally similar nanotubes of ethane and methane PMO, applied as adsorbent and particle emulsifier, have been reported by Zou et al. [72]. Moreover, powder X-ray diffraction shows a broad band at $2\theta = 1.75$, inferring a d-spacing of 5.0 nm, indicative of a degree of regularity, i.e., mesopore ordering, in the amorphous PMO framework (Fig. 1g) [73]. To confirm the apparent hollow nature of the tubes, 2D TEM analysis was extended with HAADF-STEM electron tomography (Fig. 1c) to construct a 3D visualization of the hierarchical porous network. The tomographic orthoslices (Fig. 1d) and corresponding pore volume segmentation (Fig. 1e) clearly demonstrate the hierarchical porosity of mesopores, spanning through the particle wall and culminating in a hollow central macroporous tube. Further evidence of the hollow interior of the particles is provided by Video S1, showing tomographic orthoslices and the corresponding 3D reconstruction at one end of a nanotube.

Complementary to TEM based analysis, the micro- and mesoporosity of the nanotube walls was quantified by Ar adsorption/desorption at 87 K (Fig. 1h). A fully reproducible type IV(b) isotherm (IUPAC classification) is measured, characterized by capillary condensation ($p/p_0 = 0.3$–$0.6$) in small mesopores and no hysteresis of the desorption branch [74,75]. The NLDFT-based pore size distribution and cumulative pore volume reveal the material to be largely mesoporous ($V_{meso}/V_{micro} = 11.3$), with a narrow mesopore distribution centered around 4.3 nm. A total micro- and mesopore volume and BET surface area of 0.30 $cm^3\ g^{-1}$ and 331 $m^2\ g^{-1}$ were calculated, respectively. Due to the presence of organic moieties in the silica framework, the material possesses a skeletal density of $1.88 \pm 0.04$ g $cm^{-3}$ compared to the typical 2.2 g $cm^{-3}$ of pure amorphous silica. Interestingly, mercury intrusion shows two perfectly

reproducible consecutive intrusion-extrusion cycles demonstrating the exceptionally high mechanical stability of the porous nanotubes up to 120 MPa (Fig. S6). Furthermore, the mercury intrusion-based pore size distribution shows no significant presence of pores around 150 nm in size, demonstrating that the vast majority of tubes are intact, i.e., closed at both ends. A more extended discussion of mercury porosimetry is provided in Supporting Information Section S8. Combining TEM analysis, skeletal density and micro- and mesopore volume, the volume of the hollow nanotube cavities and total pore volume were estimated to be 0.87 $cm^3\ g^{-1}$ and 1.2 $cm^3\ g^{-1}$, respectively.

Apart from porosity, surface chemistry, i.e., wettability, is regarded as a second key property in the promotive nature of a solid hydrate promoter [55–57]. Hence, a water vapor adsorption isotherm was measured at 303 K (Fig. 1i). The adsorption branch shows a slight water uptake (0.05 g $g^{-1}$) until $p/p_0 = 0.60$, which can potentially be explained by the limited presence of hydroxyl groups (1.75 OH $nm^{-2}$) along the predominantly hydrophobic pore surface of the HR-PMO material. The silanol content was estimated based on the methodology developed by Houlleberghs et al. (Section S4) and allows to classify the HR-PMO material as hydrophobic (OH $nm^{-2} < 2$) [70,76]. Unprecedently, the sigmoidal curve at $p/p_0 = 0.60$–$0.80$, characteristic for capillary condensation in hydrophobic mesopores [74], is followed by an additional increase to 0.67 g $g^{-1}$ at $p/p_0 = 0.95$, indicating partial condensation in interparticle voids or the hollow interiors of the nanotubes. In fact, the water vapor adsorption capacity at the end of capillary condensation (0.30 $cm^3\ g^{-1}$ at $p/p_{sat} = 0.80$, water density = 1 $cm^3\ g^{-1}$) perfectly matches the Ar isotherm derived total micro- and mesopore volume of 0.30 $cm^3\ g^{-1}$, indicating a total wetting of mesopores at high water vapor pressure. Furthermore, the double-stepped hysteresis loop highlights the metastability of the adsorption branch and the evaporation of condensed water from two distinct pore size ranges.

### 3.2. High-pressure methane hydrate isotherms

Before discussing results, it is worth emphasizing the different masses to which gravimetric methane storage of solid promoted hydrates can be normalized to: relative to the adsorbent mass (dry weight storage capacity $q^A_{CH_4}$), to the water mass (hydrate storage capacity $q^W_{CH_4}$), or to the total sample mass (total storage capacity $q^T_{CH_4}$). As the main focus of this manuscript is on the promoting role of HR-PMO on water to hydrate conversion, both hydrate and dry weight gravimetric storage capacity, more frequently reported in literature, are discussed in more depth [14–17,22,25,28,46,77]. Nevertheless, both are based on the total gravimetric storage capacity directly obtained from balance readings (Equation (S9), (S10) and (S11)).

As an initial screening of the hydrate promoting capabilities of HR-PMO, the optimal water loading, that is, the water loading governing a maximum absolute amount of methane uptake, was determined by uptake experiments on the gravimetric device at 248 K, imposing a pressure increase from 0.5 to 6.0 MPa at multiple fractional water loadings ($R_w = mass_{H_2O}/mass_{PMO}$) (Figs. 2a and S7). A

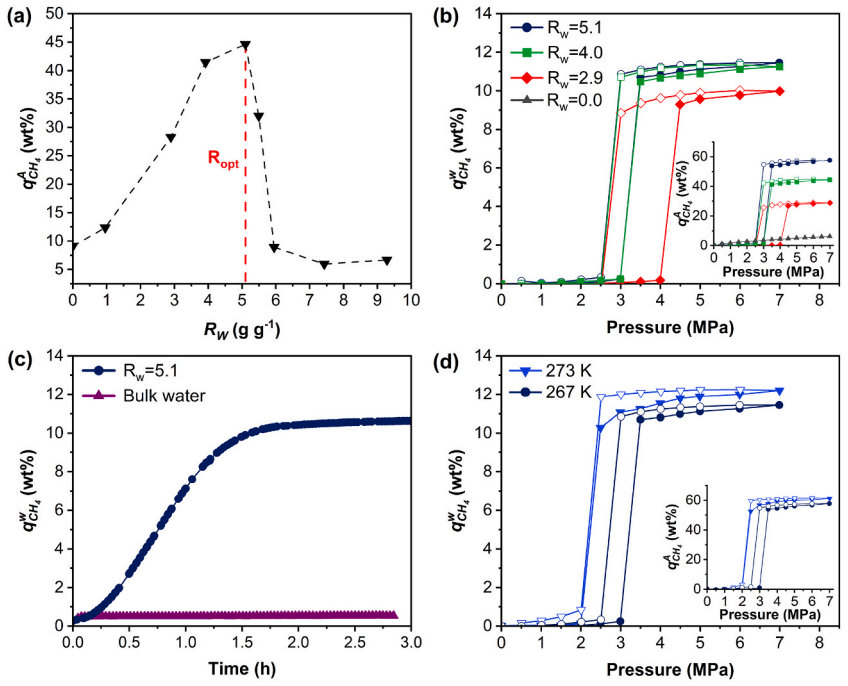


**Fig. 2.** High-pressure gravimetric methane uptake on HR-PMO. a) Dry weight storage capacity at 248 K, 6.0 MPa after 10 h equilibration as a function of water loading, with indication of the optimal water loading ($R_{opt}$). b) Methane hydrate isotherms measured for different water loadings at 273 K, expressed in hydrate and dry weight (inset) storage capacity. c) Methane uptake curves of bulk water and HR-PMO $R_w = 5.1$ for a pressure step of 3.0–3.5 MPa at 273 K. d) Methane hydrate isotherms on HR-PMO $R_w = 5.1$ at 273 K and 267 K, expressed in hydrate and dry weight (inset) storage capacity.

low temperature was adopted to conceive a large driving force for hydrate nucleation and growth, as the natural $CH_4$ hydrate phase boundary at 248 K is crossed at 1.1 MPa (Fig. S8), while both minimizing bulk hydrate formation, by the extremely slow hydrate nucleation and growth kinetics of unconfined water at 248 K. As shown in Fig. 2a, dry weight storage capacity increases with $R_w$ until a noticeably high optimal value ($R_{opt}$) of 5.1. Interestingly, this water loading exceeds the micro- and mesopore volume by a factor of 17 and the total pore volume by a factor of 4.2 (assuming $\rho_{H_2O} = 1$ g $cm^{-3}$). This indicates that not only the micro- and mesopores, but interparticle spaces, and potentially the hollow nanotube interiors, are suitable hydrate nucleation and growth environments as well. It must be emphasized that a high $R_{opt}$ will be critical to the industrial applicability of methane hydrate as a storage technology. Beyond $R_{opt}$, capacity drops drastically, most likely due to a more limited gas exchange area. Indeed, at very high water loading, slow hydrate nucleation and growth rates are expected as a bulk water system is approached [15,16,18,20].

To further elucidate the promoting effect of HR-PMO on methane hydrate formation, high-pressure methane hydrate isotherms were measured at $R_w = 2.9$, 4.0 and 5.1 up to 7.0 MPa at 273 K. As a reference, methane adsorption was measured on the dry material ($R_w = 0.0$), showing a type I shaped (IUPAC classification) isotherm with a dry weight storage capacity of 6.3 wt% at 7.0 MPa (Fig. 2b (inset) and S9) [74]. Completely different isotherm shapes are observed on humidified samples, independent of water loading (Fig. 2b). In the initial part of the isotherms, that is, before a critical clathrate formation pressure ($P_f$), almost no methane is taken up. For example, the dry weight storage capacity of HR-PMO $R_w = 5.1$ at 3.0 MPa, 273 K is merely 0.25 wt% compared to 3.69 wt% of the dry material, indicating negligible adsorption on residual porosity of the material. From a certain external methane pressure, a steep increase in methane uptake is observed, pointing at methane hydrate nucleation and growth. Beyond this critical formation pressure, methane storage only increases slightly. Similar single stepped isotherms have been reported for methane uptake on other humidified mesoporous silicas [45,47,78], however, at significantly lower water loadings ($R_w = 1.2$–2.9).

A comparison of the isotherms at different water loadings reveals a higher critical clathrate formation pressure $P_f$ at $R_w = 2.9$ (4.5 MPa) relative to $R_w = 4.0$ (3.5 MPa) and 5.1 (3.5 MPa). Furthermore, the smaller increase in gravimetric hydrate storage capacity demonstrates a reduced promoting effect at this lower water loading. Interestingly, HR-PMO loaded at $R_w = 4.0$ and 5.1 show almost coincidental isotherms over the complete formation and dissociation branches. However, the difference in absolute amount of water converted into methane hydrate, and hence methane uptake, is well visualized by expressing capacity on a dry weight basis. (Fig. 2b (inset)). At 3.5 MPa, the dry weight storage capacities are 41 wt% and 54 wt% for $R_w = 4.0$ and $R_w = 5.1$, respectively. Interestingly, this pressure is only slightly higher than the formation pressure of natural methane hydrates (2.7 MPa at 273K [79]). Moreover, at higher pressures, capacities only increase slightly, i.e. 45 wt% and 58 wt% for $R_w = 4.0$ and $R_w = 5.1$ at 7.0 MPa. Overall, although the material's storage capacity as such is not the highest reported until now, e.g. activated carbon PP-AC shows a $q^A_{CH_4}$ value of 63 wt% at 10 MPa and 275 K [15], the capacity of HR-PMO is noticeably high ($q^A_{CH_4} = 54$ wt%) for the mild operating conditions of 273 K and 3.5 MPa (further substantiated later in the discussion). This capability to efficiently enclathrate methane at low-pressure is manifested by the steep shape of the isotherm, leading to a remarkably high working capacity within a small pressure window. Based on the hydrate isotherm measurement of HR-PMO $R_w = 5.1$ at 273 K, a pressure swing of merely 1.0 MPa, between 3.5 MPa and 2.5 MPa, is sufficient to load and unload methane at $q^A_{CH_4} = 53.9$ wt% and 1.0 wt%, respectively.

Looking at the desorption branches of all three methane hydrate isotherms (Fig. 2b), significant hysteresis can be appreciated. In all cases, the storage capacity remains nearly constant between 7.0 and 3.0 MPa. Remarkably, for the 3 different water loadings, storage capacity drops drastically at the same dissociation pressure of 2.5 MPa, that is when the phase boundary of natural methane hydrate is crossed (2.7 MPa). It thus appears that, at least for these oversaturated samples, the stability of the hydrate phase is not compromised by the confining host material.

So far, the discussion has focused on equilibrium capacities, however, another very important observation is the drastically enhanced hydrate nucleation and growth rate in the presence of HR-PMO. This is demonstrated in Fig. 2c, showing a significantly faster methane uptake for HR-PMO $R_w = 5.1$ as compared to a bulk water system at 273 K and 3.5 MPa, the pressure at which the steep increase in the isotherm occurs. For the HR-PMO promoted system, 1.6 h is required to reach 95% of the equilibrium capacity ($t_{95}$) while for the bulk water system the hydrate capacity merely increases 0.2 wt% in 3 h, and hence is extremely slow. Similar equilibration times of around 1 h have been reported by Casco et al. for hydrate formation under comparable conditions (275 K and 4 MPa) and aided by petroleum-pitch derived activated carbon $R_w = 4.1$, another promising solid hydrate promoter [15,16]. Nevertheless, it is worth noting that the equilibrium dry weight storage capacity of HR-PMO is 2.7 times higher at this pressure. More details on the kinetics of methane hydrate formation in bulk water is provided in Supporting Information Section S12.

Furthermore, what is striking in the sigmoidal uptake curve of HR-PMO $R_w = 5.1$ is the absence of an initial induction/nucleation phase, as is commonly observed for solid promoted methane hydrate formation [15,16,25,26,45,46,80]. During this period, it is hypothesized that water molecules arrange around methane molecules to form the first hydrate cages, serving as initial growth centers. Overall, the immediate increase in methane storage combined with the relatively short $t_{95}$ suggests that confinement and/or distribution of water by HR-PMO is highly promoting for hydrate formation.

Given the exothermic nature of methane hydrate formation and its strong dependence on pressure and temperature, the effect of temperature on storage capacity was evaluated by an additional methane hydrate isotherm measurement on HR-PMO $R_w = 5.1$ at 267 K (Fig. 2d). The overall shape of the isotherm uptake and release branches are preserved at the lower temperature, nevertheless a slight increase in methane capacity is observed at high pressures ($q^A_{CH_4} = 62$ wt%; $q^W_{CH_4} = 12$ wt%; $q^{W_v}_{CH_4} = 139$ v $v^{-1}$ at 7.0 MPa, 267 K). However, what is more interesting is the shift of $P_f$ by 0.1 MPa, thereby making hydrate formation and dissociation occur within the same 0.5 MPa pressure window. The system thus obeys the bulk hydrate phase diagram (2.1 MPa at 267 K [79]), leading to a considerable decrease in hysteresis. From an industrial point of view this is extremely interesting, since large amounts of methane can be stored and released within a pressure-swing of 0.5 MPa. Unfortunately, formation kinetics have drastically decreased at the lower

temperature: at their respective $P_f$'s, $t_{95}$ has increased from 1.7 h to 12.4 h at 273 K compared to at 267 K, respectively. An overview of methane capacities and water to hydrate conversions at the different T and P conditions discussed, is provided by Table 1. Furthermore, a complete overview of both gravimetric and volumetric capacities for all isotherm data points is shown in Table S1.

Having discussed the promoting role of HR-PMO on both storage capacity and kinetics, it is worth comparing its performance to other solid methane hydrate promoters. Fig. 3 shows scatter plots comparing the gravimetric dry weight, hydrate, and total storage capacity of HR-PMO to 36 solid promoters from literature and to the theoretical storage capacity of pure structure I methane hydrate. Each promoter is represented by (i) a capacity at its initial hydrate formation pressure ($P_f$) and (ii) at the pressure governing a maximal $q^A_{CH_4}$ ($P_{max}$), as in most cases, this allows to study capacities in both the low- and high-pressure region. Furthermore, as a third and fourth parameter, $R_w$ and temperature were chosen, respectively. Further details on the data collection as well as exact values shown in Fig. 3, can be found in Supporting Information Section S13.

Starting the discussion with dry weight storage capacity (Fig. 3a), it may be seen that the capacity of HR-PMO (cubic markers in Fig. 3) is among the highest reported in general and is clearly superior to the other materials in the low-pressure region. Even more so, to the best of our knowledge, 54 wt% at 3.5 MPa and 273 K constitutes the highest $q^A_{CH_4}$ value reported to date under such mild conditions. This is highly promising, as being able to operate a hydrate-based storage technology with a high capacity at low pressure, i.e., near the phase transition of bulk hydrate, is not only interesting from an energy point of view, but also allows to benefit from the superior formation kinetics around the $P_f$ of a material. Indeed, several authors have recognized faster methane uptake kinetics at the initial formation point (1–2 h), compared to the kinetics at higher pressures (>10 h) [15,16,18,19,46,81].

Moving on to hydrate capacity (Fig. 3b), one can initially see that quite some materials, especially in the high-pressure, low $R_w$ region, exhibit values above the theoretical capacity of structure I methane hydrate, i.e., physically infeasible results for pure hydrate formation. However, some of these data may be explained by combined uptake through physisorption and hydrate formation. The gravimetric hydrate capacities of HR-PMO show a value slightly inferior to the theoretical maximum value of 15.5 wt%, a consequence of part of the water (26%) not being able to convert to hydrate under these conditions.

More interesting, however, is the comparison of the total gravimetric storage capacities (Fig. 3c). Among what could be called "true" solid hydrate promoters, i.e., materials showing no clear signs of physisorption, HR-PMO shows a high capacity compared to other materials, especially in the low-pressure region again. Moreover, what has been missing from the discussion until now, but is certainly relevant, is the industrial importance of the water loading. For solid promoted hydrate-based methane storage, it is reasonable to assume that the cost of the solid promoter will be of paramount importance in the economic feasibility of the technology. In this regard, a material such as HR-PMO, able of promoting hydrate formation in a mass of water 5.1 times its own weight, could imply huge cost reductions. This renders the material interesting as opposed to materials that are used at low water loadings, exhibiting higher total storage capacities.

### 3.3. Pressure swing regeneration of HR-PMO supported hydrates

As with adsorption-based methane storage, reusability is of paramount importance in the industrial application of a solid as methane hydrate promoter. The high working capacity within a narrow pressure window (steep isotherm shape) and strongly improved nucleation and growth kinetics at 273 K of HR-PMO $R_w = 5.1$ are most promising in the design of a pressure-swing storage system (Fig. S11). Therefore, cyclic pressure-based regeneration of the materials was investigated at 273 K (Fig. 4). A single gravimetric methane uptake-release experiment shows that, upon increasing the methane pressure from 2.0 MPa to 4.0 MPa, 82 min are required to achieve 95% of the equilibrium capacity ($t_{95}$) (Fig. 4a). Lowering the pressure to 2.0 MPa leads to a rapid decrease of methane storage during the first 90 min, after which no significant mass change was measured anymore (equilibrium criterion: $\Delta m_{CH_4} < 0.0001$ g for 10 min).

10 formation-dissociation cycles were performed at 273 K, composed of hydrate formation and dissociation at 4.0 and 2.0 MPa, to study the effect of repeated pressure-based regeneration on storage-release kinetics (Fig. 4c) and capacity (Fig. 4b). These cyclic experiments clearly prove the promoting effect on hydrate formation lasting over subsequent cycles. Although a slightly larger formation $t_{95}$ may be observed for cycles 2 to 10, the capacity after 2 h of pressurization is in no case less than 97% of the capacity of the first cycle. Moreover, the dissociation $t_{95}$ does not show significant differences throughout 10 cycles. These results serve as first proof of the excellent cyclic stability of the material over 10 cycles. However, to pave the way towards a future pressure-based solidified biomethane storage system, future research should be devoted to longer term cyclic experiments.

**Table 1**
Methane storage capacity and water to structure I hydrate (sI) conversion of HR-PMO at different T and P conditions.

| $R_w$ [g $g^{-1}$] | T [K] | $P_f$ [MPa] | $P_{max}$ [MPa] | $q^A_{CH_4}$ [wt%] | | $q^W_{CH_4}$ [wt%] | | $q^T_{CH_4}$ [wt%] | | sI [%][a)] | | $q^{W_v}_{CH_4}$ [v $v^{-1}$] | |
|---|---|---|---|---|---|---|---|---|---|---|---|---|---|
| | | | | $P_f$ | $P_{max}$ | $P_f$ | $P_{max}$ | $P_f$ | $P_{max}$ | $P_f$ | $P_{max}$ | $P_f$ | $P_{max}$ |
| 0.0 | 273 | n.a. | 7.0 | n.a. | 6.3 | n.a. | n.a. | n.a. | 6.3 | n.a. | n.a. | n.a. | n.a. |
| 2.9 | 273 | 4.5 | 7.0 | 26.9 | 28.9 | 9.3 | 10.0 | 6.9 | 7.4 | 60 | 64 | 109 | 116 |
| 4.0 | 273 | 3.5 | 7.0 | 41.4 | 44.5 | 10.5 | 11.3 | 8.3 | 8.9 | 68 | 73 | 121 | 130 |
| 5.1 | 273 | 3.5 | 7.0 | 53.9 | 57.7 | 10.7 | 11.5 | 8.9 | 9.5 | 69 | 74 | 124 | 132 |
| 5.1 | 267 | 2.5 | 7.0 | 52.6 | 61.4 | 10.3 | 12.2 | 8.6 | 10.0 | 66 | 79 | 119 | 139 |

[a)] Based on structure I methane hydrate stoichiometry of 1 $CH_4$. 5.75$H_2O$ or gravimetric storage capacity of 15.5 g $CH_4$/100 g $H_2O$.

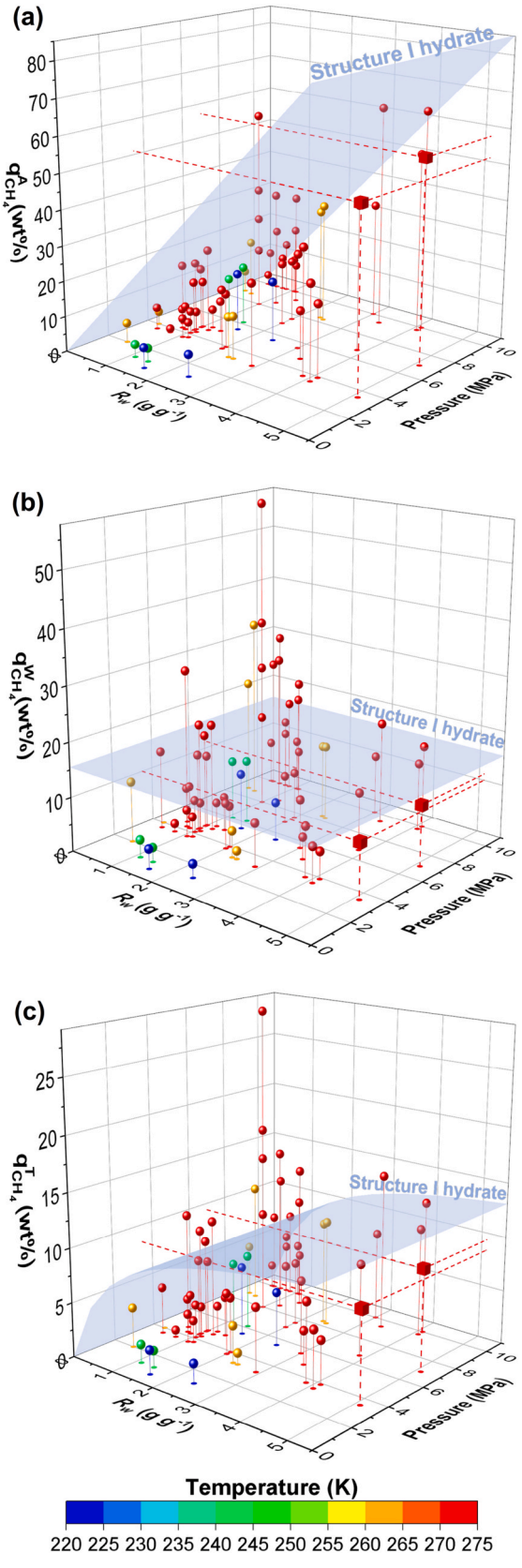


*(caption on next page)*

**Fig. 3.** Comparison of HR-PMO to 36 literature reported solid promoters in terms of a) dry weight, b) hydrate and c) total storage capacity. Values of HR-PMO are represented by cubic markers and dashed red drop lines. The theoretical storage capacity of structure I methane hydrate is shown by a light blue surface. (For interpretation of the references to colour in this figure legend, the reader is referred to the Web version of this article.)

### *3.4. Visualization of methane storage in hydrate*

To confirm storage of methane in a clathrate hydrate structure, the gravimetric methane uptake results are complemented with PXRD measurements. The reference X-ray diffraction spectrum of HR-PMO $R_w = 0.0$ inside the Kapton® reinforced XRD sample holder reveals no identifiable reflections (Fig. S12). PXRD of HR-PMO $R_w = 5.1$ subjected to 7.0 MPa methane pressure at 273 K, however, shows main reflections attributable to hexagonal ice (Ih) and a second crystalline phase that can be indexed using a cubic unit cell (Pm3n) with lattice constant a = 11.97 Å, i.e., the crystal structure of a structure I (sI) clathrate hydrate (Fig. 5a). The presence of hexagonal ice may come as no surprise, since the high-pressure methane hydrate isotherms had already shown a 74% conversion of water to hydrate under these conditions.

To achieve a better understanding of the confining spaces promoting methane hydrate formation and of the distribution of water throughout the hierarchical pore structure, cryogenic 2D-TEM and tomography of HR-PMO $R_w = 5.1$ subjected to 7.0 MPa methane at 273 K, were performed, to our knowledge for the first time in gas hydrate science literature. Comparing TEM images of HR-PMO in the presence and absence of hydrate, Fig. 1a and b and 5b,c, respectively, shows filling of some of the nanotubes, presumably by structure I methane hydrate or hexagonal ice, as was evidenced by the PXRD results (Fig. 5a). The presence is further appreciated by inspection of the contrast of the nanotubes indicated by yellow arrows in Fig. 5b. In addition, beam sensitive protrusions may as well be observed on the external surface of the nanotubes (Fig. 5c). Tomography-based sample reconstruction further confirms the integral dispersion of the filling through the nanotube structures (Fig. 5d and Video S2). For two nanotubes, the hollow cavity is filled, while for the third one, only protrusion can be observed on the internal and external surface of the particles. Interestingly, both the STEM and tomography images do not show any bulk crystallinity present other than in/on the nanotubes. It thus appears that at a water loading exceeding the total pore volume 4.2 times, water is well distributed throughout the porous nanotubes, i.e., confined inside the hollow nanotube cavities and wall porosity as well as dispersed on the large external surface of the nanotubes. Hence, these observations directly explain the apparent dry state (Fig. S5) and promoting effect of HR-PMO on methane hydrate nucleation and growth kinetics, even at high water loading.

Overall, considering most of the water is converted to hydrate, and taking into account the X-ray spectroscopic evidence of its structure I crystallinity, one can conclude the majority of crystallinity observed on 2D-STEM and tomography figures must be methane hydrate dispersed throughout the nanotubes.

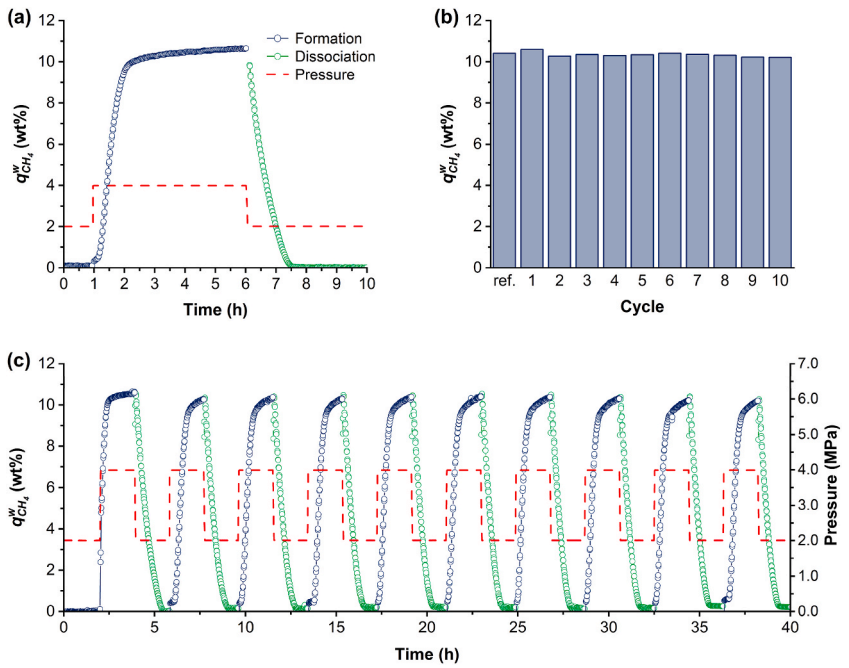


**Fig. 4.** a, c) Gravimetric uptake-release experiments on HR-PMO $R_w = 5.1$ at 273 K by an increase in methane pressure from 2.0 MPa to 4.0 MPa (uptake) and pressure decrease back to 2.0 MPa (release). The methane pressure was kept at 4.0 MPa and 2.0 MPa for 5 h each in experiment a) and for 2 h each in all cycles of experiment c). b) The gravimetric methane storage capacity of each cycle shown in a) and c).

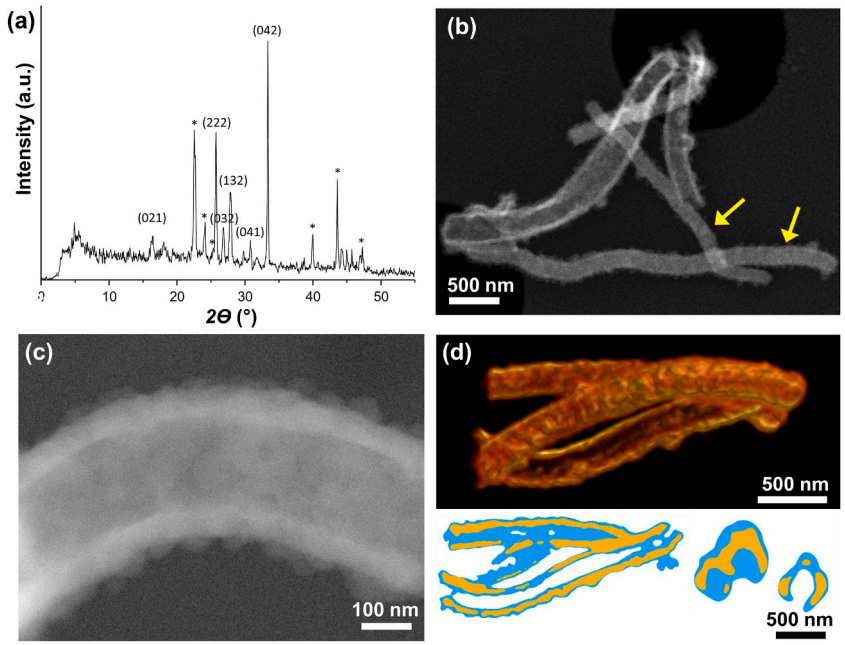


**Fig. 5.** a) XRD-spectrum of HR-PMO $R_w = 5.1$ subjected to 7.0 MPa methane at 273 K, determined under cryogenic conditions. Reflections characteristic of structure I clathrate hydrate are denoted by their corresponding miller indices (hkl). Reflections originating from hexagonal ice (P63/mmc; a = 4.4980 Å, c = 7.3224 Å) are highlighted with an asterisk (*). The intensity of hexagonal ice is exacerbated using liquid nitrogen as refrigerant, promoting water condensation and subsequent ice formation from water vapor in the air. b) HAADF-STEM image where filled nanotubes can be distinguished from the empty ones due to their homogeneous contrast. c) HAADF-STEM image of protrusions on the nanotube walls. d) 3D rendering of the outcome of the volume reconstructed by HAADF-STEM tomography and perpendicular orthoslices of the segmented 3D volume clearly showing an empty nanotube along with two filled ones (HR-PMO: orange; filling: blue). (For interpretation of the references to colour in this figure legend, the reader is referred to the Web version of this article.)

## 4. Conclusion

The promoting impact of ring PMO nanotubes on methane hydrate nucleation and growth was investigated. High-pressure gravimetric methane uptake measurements on HR-PMO, humidified in different water-to-adsorbent mass ratio's $R_w$, indicated a ratio of 5.1 to be optimal for methane uptake. Further investigation of the pressure dependency of hydrate formation at 273 K showed single-stepped isotherm shapes, with steep increases at 3.5 MPa (samples $R_w = 4.0$ and 5.1), close to the formation pressure of bulk hydrate. By comparing the gravimetric dry weight, hydrate and total storage capacity of HR-PMO $R_w = 5.1$ to literature-reported promoters, it was shown that the material is highly promising in terms of equilibrium capacity, especially in the low-pressure region ($q^{A}_{CH_4} = 53.9$ wt%, $q^{W}_{CH_4} = 10.7$ wt%, $q^{T}_{CH_4} = 8.9$ wt% at 3.5 MPa, 273 K). Moreover, dynamic high-pressure gravimetric measurements further demonstrated the strongly enhanced formation kinetics, without any detectable nucleation period, in presence of HR-PMO. The single-stepped shape of the isotherm towards a high methane storage capacity at mild working conditions, the narrow hysteresis loop and the material's potential to drastically improve hydrate formations rates are highly encouraging in the development of solid aided hydrate-based methane storage. Hence, the applicability of wetted HR-PMO as storage medium was proven through multiple pressure-induced formation-dissociation cycles, showing only minor losses in storage capacity (97% preservation of original capacity). Lastly, high-pressure uptake measurements were complemented with PXRD, confirming the presence of structure I methane hydrate, and cryo-tomography, showing the distribution and confinement of water in mesopores of the outer wall, along the central channels of the nanotubes and on the external nanotube surface.

## Author contribution statement

Emile Jules Beckwée, Geert Watson, Maarten Houlleberghs: Conceived and designed the experiments; Performed the experiments; Analyzed and interpreted the data; Wrote the paper.

Daniel Arenas Esteban: Performed the experiments; Analyzed and interpreted the data.

Sara Bals, Pascal Van Der Voort: Contributed reagents, materials, analysis tools or data.

Eric Breynaert, Johan Martens: Contributed reagents, materials, analysis tools or data; Wrote the paper.

Gino V. Baron: Conceived and designed the experiments; Performed the experiments; Analyzed and interpreted the data.

Joeri F.M. Denayer: Contributed reagents, materials, analysis tools or data; Analyzed and interpreted the data; Wrote the paper.

## Data availability statement

Data included in article/supp. material/referenced in article.

## Declaration of competing interest

The authors declare that they have no known competing financial interests or personal relationships that could have appeared to influence the work reported in this paper

## Acknowledgements

E.J.B., G.W. and M.H. contributed equally to this work. M.H. acknowledges FWO for an FWO-SB fellowship. All authors acknowledge VLAIO for Moonshot funding (ARCLATH, n° HBC.2019.0110, ARCLATH2, n° HBC.2021.0254). J.A.M. acknowledges the Flemish Government for long-term structural funding (Methusalem) and department EWI for infrastructure investment via the Hermes Fund (AH.2016.134). NMRCoRe acknowledges the Flemish government, department EWI for financial support as International Research Infrastructure (I001321N: Nuclear Magnetic Resonance Spectroscopy Platform for Molecular Water Research). J.A.M. acknowledges the European Research Council (ERC) for an Advanced Research Grant under the European Union's Horizon 2020 research and innovation program under grant agreement No. 834134 (WATUSO). S.B acknowledges financial support by the Research Foundation Flanders (FWO grant G.0381.16N). This project also received funding from the European Union's Horizon 2020 research and innovation program under grant agreement No 731019 (EUSMI) and No 815128 (REALNANO).

## Appendix A. Supplementary data

Supplementary data to this article can be found online at https://doi.org/10.1016/j.heliyon.2023.e17662.

## References

[1] I. Angelidaki, L. Treu, P. Tsapekos, G. Luo, S. Campanaro, H. Wenzel, P.G. Kougias, Biogas upgrading and utilization: current status and perspectives, Biotechnol. Adv. 36 (2018) 452–466, https://doi.org/10.1016/j.biotechadv.2018.01.011.
[2] H.P. Veluswamy, A. Kumar, Y. Seo, J.D. Lee, P. Linga, A review of solidified natural gas (SNG) technology for gas storage via clathrate hydrates, Appl. Energy 216 (2018) 262–285, https://doi.org/10.1016/j.apenergy.2018.02.059.
[3] E.D. Sloan Jr., Fundamental principles and applications of natural gas hydrates, Nature 426 (2003) 353–359, https://doi.org/10.1038/nature02135.
[4] A.H. Johnson, Global ResouRce Potential of Gas HydRate-A New Calculation, MEthane Hydrate Newsl, vol. 11, 2011, pp. 1–4. http://www.netl (accessed May 31, 2022).
[5] R. Boswell, T.S. Collett, Current perspectives on gas hydrate resources, Energy Environ. Sci. 4 (2011) 1206–1215, https://doi.org/10.1039/c0ee00203h.
[6] C. Ruppel, Permafrost-associated gas hydrate: is it really approximately 1 % of the global system? J. Chem. Eng. Data 60 (2015) 429–436, https://doi.org/10.1021/JE500770M/ASSET/IMAGES/LARGE/JE-2014-00770M_0004.JPEG.
[7] G.R. Dickens, Down the Rabbit Hole: toward appropriate discussion of methane release from gas hydrate systems during the Paleocene-Eocene thermal maximum and other past hyperthermal events, Clim. Past 7 (2011) 831–846, https://doi.org/10.5194/cp-7-831-2011.
[8] E. Dendy Sloan, C.A. Koh, "9078_C000"-2007/8/1-20:50-page i-#1 Clathrate Hydrates of Natural Gases, 3th edition, CRC Press, Boca Raton, 2008.
[9] A.Y. Manakov, N. V Penkov, T. V Rodionova, A.N. Nesterov, E.E. Fesenko Jr., Kinetics of formation and dissociation of gas hydrates, Russ. Chem. Rev. 86 (2017) 845–869, https://doi.org/10.1070/rcr4720.
[10] A. Kumar, G. Bhattacharjee, B.D. Kulkarni, R. Kumar, Role of surfactants in promoting gas hydrate formation, Ind. Eng. Chem. Res. 54 (2015) 12217–12232, https://doi.org/10.1021/acs.iecr.5b03476.
[11] A. Mohammadi, M. Manteghian, A.H. Mohammadi, A. Jahangiri, Induction time, storage capacity, and rate of methane hydrate formation in the presence of SDS and silver nanoparticles, Chem. Eng. Commun. 204 (2017) 1420–1427, https://doi.org/10.1080/00986445.2017.1366903.
[12] J. Lee, Y.K. Jin, Y. Seo, Characterization of cyclopentane clathrates with gaseous guests for gas storage and separation, Chem. Eng. J. 338 (2018) 572–578, https://doi.org/10.1016/j.cej.2018.01.054.
[13] H.P. Veluswamy, A.J.H. Wong, P. Babu, R. Kumar, S. Kulprathipanja, P. Rangsunvigit, P. Linga, Rapid methane hydrate formation to develop a cost effective large scale energy storage system, Chem. Eng. J. 290 (2016) 161–173, https://doi.org/10.1016/j.cej.2016.01.026.
[14] M.E. Casco, E. Zhang, S. Grätz, S. Krause, V. Bon, D. Wallacher, N. Grimm, D.M. Többens, T. Hauß, L. Borchardt, Experimental evidence of confined methane hydrate in hydrophilic and hydrophobic model carbons, J. Phys. Chem. C 123 (2019) 24071–24079, https://doi.org/10.1021/acs.jpcc.9b06366.
[15] M.E. Casco, J. Silvestre-Albero, A.J. Ramírez-Cuesta, F. Rey, J.L. Jordá, A. Bansode, A. Urakawa, I. Peral, M. Martínez-Escandell, K. Kaneko, F. Rodríguez-Reinoso, Methane hydrate formation in confined nanospace can surpass nature, Nat. Commun. 6 (2015) 1–8, https://doi.org/10.1038/ncomms7432.
[16] M.E. Casco, C. Cuadrado-Collados, M. Martínez-Escandell, F. Rodríguez-Reinoso, J. Silvestre-Albero, Influence of the oxygen-containing surface functional groups in the methane hydrate nucleation and growth in nanoporous carbon, Carbon N. Y. 123 (2017) 299–301, https://doi.org/10.1016/j.carbon.2017.07.061.
[17] C. Cuadrado-Collados, F. Fauth, I. Such-Basañez, M. Martínez-Escandell, J. Silvestre-Albero, Methane hydrate formation in the confined nanospace of activated carbons in seawater environment, Microporous Mesoporous Mater. 255 (2018) 220–225, https://doi.org/10.1016/j.micromeso.2017.07.047.
[18] A. Celzard, J.F. Marêché, Optimal wetting of active carbons for methane hydrate formation, Fuel 85 (2006) 957–966, https://doi.org/10.1016/j.fuel.2005.10.019.
[19] A. Perrin, A. Celzard, J.F. Marêché, G. Furdin, Methane storage within dry and wet active carbons: a comparative study, Energy Fuel. 17 (2003) 1283–1291, https://doi.org/10.1021/ef030067i.
[20] L. Zhou, Y. Sun, Y. Zhou, Enhancement of the methane storage on activated carbon by preadsorbed water, AIChE J. 48 (2002) 2412–2416, https://doi.org/10.1002/aic.690481030.
[21] M.J.D. Mahboub, A. Ahmadpour, H. Rashidi, Improving methane storage on wet activated carbons at various amounts of water, Ranliao Huaxue Xuebao/J. Fuel Chem. Technol. 40 (2012) 385–389, https://doi.org/10.1016/s1872-5813(12)60017-6.

[22] L. Borchardt, W. Nickel, M. Casco, I. Senkovska, V. Bon, D. Wallacher, N. Grimm, S. Krause, J. Silvestre-Albero, Illuminating solid gas storage in confined spaces – methane hydrate formation in porous model carbons, Phys. Chem. Chem. Phys. 18 (2016) 20607–20614, https://doi.org/10.1039/C6CP03993F.

[23] L. Yan, G. Chen, W. Pang, J. Liu, Experimental and modeling study on hydrate formation in wet activated carbon, J. Phys. Chem. B 109 (2005) 6025–6030, https://doi.org/10.1021/jp045679y.

[24] A. Siangsai, P. Rangsunvigit, B. Kitiyanan, S. Kulprathipanja, P. Linga, Investigation on the roles of activated carbon particle sizes on methane hydrate formation and dissociation, Chem. Eng. Sci. 126 (2015) 383–389, https://doi.org/10.1016/J.CES.2014.12.047.

[25] M.E. Casco, F. Rey, J.L. Jordá, S. Rudić, F. Fauth, M. Martínez-Escandell, F. Rodríguez-Reinoso, E.V. Ramos-Fernández, J. Silvestre-Albero, Paving the way for methane hydrate formation on metal-organic frameworks (MOFs), Chem. Sci. 7 (2016) 3658–3666, https://doi.org/10.1039/c6sc00272b.

[26] L. Mu, B. Liu, H. Liu, Y. Yang, C. Sun, G. Chen, A novel method to improve the gas storage capacity of ZIF-8, J. Mater. Chem. 22 (2012) 12246–12252, https://doi.org/10.1039/c2jm31541f.

[27] S. Denning, A.A.A. Majid, J.M. Lucero, J.M. Crawford, M.A. Carreon, C.A. Koh, Metal-organic framework HKUST-1 promotes methane hydrate formation for improved gas storage capacity, ACS Appl. Mater. Interfaces 12 (2020) 53510–53518, https://doi.org/10.1021/acsami.0c15675.

[28] C. Cuadrado-Collados, G. Mouchaham, L. Daemen, Y. Cheng, A. Ramirez-Cuesta, H. Aggarwal, A. Missyul, M. Eddaoudi, Y. Belmabkhout, J. Silvestre-Albero, Quest for an optimal methane hydrate formation in the pores of hydrolytically stable metal-organic frameworks, J. Am. Chem. Soc. 142 (2020) 13391–13397, https://doi.org/10.1021/jacs.0c01459.

[29] D. Kim, Y.H. Ahn, H. Lee, Phase equilibria of CO2 and CH4 hydrates in intergranular meso/macro pores of MIL-53 metal organic framework, J. Chem. Eng. Data 60 (2015) 2178–2185, https://doi.org/10.1021/acs.jced.5b00322.

[30] E. Andres-Garcia, A. Dikhtiarenko, F. Fauth, J. Silvestre-Albero, E.V. Ramos-Fernández, J. Gascon, A. Corma, F. Kapteijn, Methane hydrates: nucleation in microporous materials, Chem. Eng. J. 360 (2019) 569–576, https://doi.org/10.1016/j.cej.2018.11.216.

[31] X. Zang, J. Du, D. Liang, S. Fan, C. Tang, Influence of A-type zeolite on methane hydrate formation, Chin. J. Chem. Eng. 17 (2009) 854–859, https://doi.org/10.1016/S1004-9541(08)60287-6.

[32] D.L. Zhong, Z. Li, Y.Y. Lu, J. Le Wang, J. Yan, S.L. Qing, Investigation of $CO_2$ capture from a $CO_2 + CH_4$ gas mixture by gas hydrate formation in the fixed bed of a molecular sieve, Ind. Eng. Chem. Res. 55 (2016) 7973–7980, https://doi.org/10.1021/acs.iecr.5b03989.

[33] Y. Zhao, J. Zhao, W. Liang, Q. Gao, D. Yang, Semi-clathrate hydrate process of methane in porous media-microporous materials of 5A-type zeolites, Fuel 220 (2018) 185–191, https://doi.org/10.1016/j.fuel.2018.01.067.

[34] U. Karaaslan, M. Parlaktuna, Promotion effect of polymers and surfactants on hydrate formation rate, Energy Fuel. 16 (2002) 1413–1416, https://doi.org/10.1021/ef020023u.

[35] M.T. Sun, F.P. Song, G.D. Zhang, J.Z. Li, F. Wang, Polymeric superabsorbent hydrogel-based kinetic promotion for gas hydrate formation, Fuel 288 (2021), 119676, https://doi.org/10.1016/j.fuel.2020.119676.

[36] P. Linga, C. Haligva, S.C. Nam, J.A. Ripmeester, P. Englezos, Gas hydrate formation in a variable volume bed of silica sand particles, Energy Fuel. 23 (2009) 5496–5507, https://doi.org/10.1021/ef900542m.

[37] T. Uchida, T. Ebinuma, T. Ishizaki, Dissociation condition measurements of methane hydrate in confined small pores of porous glass, J. Phys. Chem. B 103 (1999) 3659–3662, https://doi.org/10.1021/jp9845591.

[38] F. Filarsky, C. Schmuck, H.J. Schultz, Impact of modified silica beads on methane hydrate formation in a fixed-bed reactor, Ind. Eng. Chem. Res. 58 (2019) 16687–16695, https://doi.org/10.1021/acs.iecr.9b01952.

[39] Z.R. Chong, M. Yang, B.C. Khoo, P. Linga, Size effect of porous media on methane hydrate formation and dissociation in an excess gas environment, Ind. Eng. Chem. Res. 55 (2016) 7981–7991, https://doi.org/10.1021/acs.iecr.5b03908.

[40] V.C. Nair, S. Ramesh, G.A. Ramadass, J.S. Sangwai, Influence of thermal stimulation on the methane hydrate dissociation in porous media under confined reservoir, J. Pet. Sci. Eng. 147 (2016) 547–559, https://doi.org/10.1016/j.petrol.2016.09.017.

[41] Y.P. Handa, D. Stupin, Thermodynamic properties and dissociation characteristics of methane and propane hydrates in 70-Å-radius silica gel pores, J. Phys. Chem. 96 (1992) 8599–8603, https://doi.org/10.1021/j100200a071.

[42] Y. Seo, H. Lee, T. Uchida, Methane and carbon dioxide hydrate phase behavior in small porous silica gels: three-phase equilibrium determination and thermodynamic modeling, Langmuir 18 (2002) 9164–9170, https://doi.org/10.1021/la0257844.

[43] K. Inkong, H.P. Veluswamy, P. Rangsunvigit, S. Kulprathipanja, P. Linga, Innovative approach to enhance the methane hydrate formation at near-ambient temperature and moderate pressure for gas storage applications, Ind. Eng. Chem. Res. 58 (2019) 22178–22192, https://doi.org/10.1021/acs.iecr.9b04498.

[44] D.H. Smith, J.W. Wilder, K. Seshadri, Methane hydrate equilibria in silica gels with broad pore-size distributions, AIChE J. 48 (2002) 393–400, https://doi.org/10.1002/aic.690480222.

[45] L. Zhou, X. Liu, Y. Sun, J. Li, Y. Zhou, Methane sorption in ordered mesoporous silica SBA-15 in the presence of water, J. Phys. Chem. B 109 (2005) 22710–22714, https://doi.org/10.1021/JP0546002/ASSET/IMAGES/LARGE/JP0546002F00011.JPEG.

[46] M.E. Casco, S. Grätz, D. Wallacher, N. Grimm, D.M. Többens, M. Bilo, N. Speil, M. Fröba, L. Borchardt, Influence of surface wettability on methane hydrate formation in hydrophilic and hydrophobic mesoporous silicas, Chem. Eng. J. 405 (2021), 126955, https://doi.org/10.1016/j.cej.2020.126955.

[47] X. Liu, D. Liu, W. Xie, X. Cui, Y. Chen, Methane hydrate uptake of MCM-41 mesoporous molecular sieves with preadsorbed water, J. Chem. Eng. Data 63 (2018) 1767–1772, https://doi.org/10.1021/acs.jced.8b00060.

[48] D.L. Zhong, S.Y. He, D.J. Sun, C. Yang, Comparison of methane hydrate formation in stirred reactor and porous media in the presence of SDS, Energy Proc. 61 (2014) 1573–1576, https://doi.org/10.1016/j.egypro.2014.12.174.

[49] B.O. Carter, W. Wang, D.J. Adams, A.I. Cooper, Gas storage in “dry water” and “dry gel” clathrates, Langmuir 26 (2010) 3186–3193, https://doi.org/10.1021/LA903120P/SUPPL_FILE/LA903120P_SI_001.PDF.

[50] W. Wang, C.L. Bray, D.J. Adams, A.I. Cooper, Methane storage in dry water gas hydrates, J. Am. Chem. Soc. 130 (2008) 11608–11609, https://doi.org/10.1021/JA8048173.

[51] J. Park, K. Shin, J. Kim, H. Lee, Y. Seo, N. Maeda, W. Tian, C.D. Wood, Effect of hydrate shell formation on the stability of dry water, J. Phys. Chem. C 119 (2015) 1690–1699, https://doi.org/10.1021/JP510603Q/SUPPL_FILE/JP510603Q_SI_001.PDF.

[52] S. Fan, L. Yang, Y. Wang, X. Lang, Y. Wen, X. Lou, Rapid and high capacity methane storage in clathrate hydrates using surfactant dry solution, Chem. Eng. Sci. 106 (2014) 53–59, https://doi.org/10.1016/J.CES.2013.11.032.

[53] J. Wang, R. Wang, R.H. Yoon, Y. Seol, Use of hydrophobic particles as kinetic promoters for gas hydrate formation, J. Chem. Eng. Data 60 (2015) 383–388, https://doi.org/10.1021/je5006455.

[54] H. Li, L. Wang, Hydrophobized particles can accelerate nucleation of clathrate hydrates, Fuel 140 (2015) 440–445, https://doi.org/10.1016/j.fuel.2014.10.005.

[55] L. Borchardt, M.E. Casco, J. Silvestre-Albero, Methane hydrate in confined spaces: an alternative storage system, ChemPhysChem 19 (2018) 1298–1314, https://doi.org/10.1002/cphc.201701250.

[56] N.N. Nguyen, M. Galib, A.V. Nguyen, Critical review on gas hydrate formation at solid surfaces and in confined spaces - why and how does interfacial regime matter? Energy Fuel. 34 (2020) 6751–6760, https://doi.org/10.1021/acs.energyfuels.0c01291.

[57] P. Mileo, S.M.J. Rogge, M. Houlleberghs, E. Breynaert, J. Martens, V. Van Speybroeck, Interfacial study of clathrates confined in reversed silica pores, J. Mater. Chem. (2021), https://doi.org/10.1039/d1ta03105h.

[58] W. Wang, C.L. Bray, D.J. Adams, A.I. Cooper, Methane storage in dry water gas hydrates, J. Am. Chem. Soc. 130 (2008) 11608–11609, https://doi.org/10.1021/ja8048173.

[59] N.N. Nguyen, A.V. Nguyen, K.M. Steel, L.X. Dang, M. Galib, Interfacial gas enrichment at hydrophobic surfaces and the origin of promotion of gas hydrate formation by hydrophobic solid particles, J. Phys. Chem. C 121 (2017) 3830–3840, https://doi.org/10.1021/acs.jpcc.6b07136.

[60] Y. Wei, X. Li, R. Zhang, Y. Liu, W. Wang, Y. Ling, A.M. El-Toni, D. Zhao, Periodic mesoporous organosilica nanocubes with ultrahigh surface areas for efficient CO2 adsorption, Sci. Rep. 6 (2016) 1–11, https://doi.org/10.1038/srep20769.

[61] P. Van Der Voort, D. Esquivel, E. De Canck, F. Goethals, I. Van Driessche, S.S. Francisco Romero, Periodic Mesoporous Organosilicas: from simple to complex bridges; a comprehensive overview of functions, morphologies and applications, Chem. Soc. Rev. 42 (2013) 3913–3955, https://doi.org/10.1039/C2CS35222B.

[62] W. Guo, X. Li, X.S. Zhao, Understanding the hydrothermal stability of large-pore periodic mesoporous organosilicas and pure silicas, Microporous Mesoporous Mater. 93 (2006) 285–293, https://doi.org/10.1016/J.MICROMESO.2006.03.009.

[63] M. Kruk, Access to ultralarge-pore ordered mesoporous materials through selection of surfactant/swelling-agent micellar templates, Acc. Chem. Res. 45 (2012) 1678–1687, https://doi.org/10.1021/ar200343s.

[64] S. Soltani, N. Khanian, U. Rashid, T.S. Yaw Choong, Fundamentals and recent progress relating to the fabrication, functionalization and characterization of mesostructured materials using diverse synthetic methodologies, RSC Adv. 10 (2020) 16431–16456, https://doi.org/10.1039/d0ra00440e.

[65] W. van Aarle, W.J. Palenstijn, J. De Beenhouwer, T. Altantzis, S. Bals, K.J. Batenburg, J. Sijbers, The ASTRA Toolbox: a platform for advanced algorithm development in electron tomography, Ultramicroscopy 157 (2015) 35–47, https://doi.org/10.1016/J.ULTRAMIC.2015.05.002.

[66] W. Van Aarle, W. Jan Palenstijn, J. Cant, E. Janssens, F. Bleichrodt, A. Dabravolski, J. DE Beenhouwer, K. Joost Batenburg, J. Sijbers, E. Perilli, V. Le, B. Ma, P. Salmon, K. Reynolds, G.H. Erbou, M. Vester-Christensen, M.F. Hansen, M. Darré, M. Hviid, E. V Olsen, V. Aarle, W.J. Palenstijn, J. De Beenhouwer, T. Altantzis, S. Bals, K.J. Batenburg, J. Sijbers, T. Astra, A. Sheppard, S. Latham, J. Middleton, A. Kingston, G. Myers, T. Varslot, A. Fogden, T. Sawkins, R. Cruikshank, M. Saadatfar, N. Francois, C. Arns, T. Senden, A. Mirone, E. Brun, E. Gouillart, P. Tafforeau, J. Kieffer, D.M. Pelt, D. Gürsoy, F. De Carlo, C. B. Reid, M.M. Betcke, D. Chana, R.D. Speller, Fast and flexible X-ray tomography using the ASTRA toolbox, Opt Express 24 (22) (2016) 25129–25147, https://doi.org/10.1364/OE.24.025129.

[67] F. Rouquerol, J. Rouquerol, K.S.W. Sing, P. Llewellyn, G. Maurin, Adsorption by Powders and Porous Solids, second ed., Academic Press, London, 2013 https://doi.org/10.1016/b978-0-12-598920-6.x5000-3.

[68] J. Rouquerol, P. Llewellyn, F. Rouquerol, Is the BET Equation Applicable to Microporous Adsorbents? Elsevier B.V., 2007 https://doi.org/10.1016/s0167-2991(07)80008-5.

[69] S. Brunauer, P.H. Emmett, E. Teller, Adsorption of gases in multimolecular layers, J. Am. Chem. Soc. 60 (1938) 309–319, https://doi.org/10.1021/ja01269a023.

[70] M. Houlleberghs, A. Hoffmann, D. Dom, C.E.A. Kirschhock, F. Taulelle, J.A. Martens, E. Breynaert, Absolute quantification of water in microporous solids with 1 H magic angle spinning NMR and standard addition, Anal. Chem. 89 (2017) 14, https://doi.org/10.1021/acs.analchem.7b01653.

[71] H. Vanrompay, A. Skorikov, E. Bladt, A. Béché, B. Freitag, J. Verbeeck, S. Bals, Fast versus conventional HAADF-STEM tomography of nanoparticles: advantages and challenges, Ultramicroscopy 221 (2021), https://doi.org/10.1016/j.ultramic.2020.113191.

[72] H. Zou, R. Wang, Z. Shi, J. Dai, Z. Zhang, S. Qiu, One-dimensional periodic mesoporous organosilica helical nanotubes with amphiphilic properties for the removal of contaminants from water, J. Mater. Chem. A. 4 (2016) 4145–4154, https://doi.org/10.1039/c6ta00708b.

[73] K. Landskron, B.D. Hatton, D.D. Perovic, G.A. Ozin, Periodic mesoporous organosilicas containing interconnected $[Si(CH_2)]_3$ rings, Science (80-.) 302 (2003), https://doi.org/10.1126/science.1084973.

[74] M. Thommes, K. Kaneko, A.V. Neimark, J.P. Olivier, F. Rodriguez-Reinoso, J. Rouquerol, K.S.W. Sing, Physisorption of gases, with special reference to the evaluation of surface area and pore size distribution (IUPAC Technical Report), Pure Appl. Chem. 87 (2015) 1051–1069, https://doi.org/10.1515/pac-2014-1117.

[75] C. Schlumberger, M. Thommes, Characterization of hierarchically ordered porous materials by physisorption and mercury porosimetry—a tutorial review, Adv. Mater. Interfac. 8 (2021), 2002181, https://doi.org/10.1002/admi.202002181.

[76] J.D. Cyran, M.A. Donovan, D. Vollmer, F.S. Brigiano, S. Pezzotti, D.R. Galimberti, M.P. Gaigeot, M. Bonn, E.H.G. Backus, Molecular hydrophobicity at a macroscopically hydrophilic surface, Proc. Natl. Acad. Sci. U.S.A. 116 (2019) 1520–1525, https://doi.org/10.1073/pnas.1819000116.

[77] C. Cuadrado-Collados, J. Farrando-Pérez, M. Martínez-Escandell, L.A. Ramírez-Montoya, J.A. Menéndez, A. Arenillas, M.A. Montes-Morán, J. Silvestre-Albero, Well-defined meso/macroporous materials as a host structure for methane hydrate formation: organic versus carbon xerogels, Chem. Eng. J. 402 (2020), 126276, https://doi.org/10.1016/j.cej.2020.126276.

[78] L. Zhou, X. Liu, J. Li, Y. Sun, Y. Zhou, Sorption/desorption equilibrium of methane in silica gel with pre-adsorption of water, Colloids Surfaces A Physicochem. Eng. Asp. 273 (2006) 117–120, https://doi.org/10.1016/j.colsurfa.2005.08.017.

[79] K. Kroenlein, C.D. Muzny, A. Kazakov, V.V. Diky, R.D. Chirico, E.D. Sloan, M. Frenkel, Clathrate hydrate physical property database, Natl. Energy Technol. Lab. U.S. Dep. Energy. 200 (2009). http://gashydrates.nist.gov/.

[80] C. Chen, Y. Li, J. Cao, Methane hydrate formation in hollow ZIF-8 nanoparticles for improved methane storage capacity, Catalysts 12 (2022) 1–13, https://doi.org/10.3390/catal12050485.

[81] L. Borchardt, M.E. Casco, J. Silvestre-Albero, Methane hydrate in confined spaces: an alternative storage system, ChemPhysChem 19 (2018) 1298–1314, https://doi.org/10.1002/cphc.201701250.